RESEARCH ARTICLE

Editor's Choice

ADVANCED ENGINEERING MATERIALS

www.aem-journal.com

(Nb,Ti)(C,N)-Precipitates in High-Strength Low-Alloyed Steels—Modeling, Characterization and Validation

Marc Laub, Christian Motz, Eric Detemple, and Sebastian Scholl*

The chemical composition and microstructural evolution during thermomechanical treatments of high-strength low-alloy steels containing Nb and Ti determine the mechanical properties. To optimize processing and heat treatment, it is important to characterize the microstructures and to understand how the mechanical properties are affected by the different elements of the microstructures. Herein, it has been attempted to investigate the nucleation and growth of niobium–titanium carbonitrides using transmission electron microscopy (TEM)-energy-dispersive X-ray spectroscopy measurements. Since TEM measurements alone tend to suffer from poor statistics, an attempt is made to establish a kinetic/thermodynamic model that is representative for larger volumes of material while giving fair credit to the local TEM results. The present work goes beyond the simulation of temperature-dependent average compositional changes of precipitates. Instead, this study aims to capture the entire compositional spectrum of precipitates and their evolution during processing and heat treatment. The model used is based on the CALPHAD approach but has been extended by a Monte Carlo approach. The focus is on the rationalization of particle compositions that are experimentally observable by TEM and cannot be obtained by conventional mean-field models based on extremum principles.

1. Introduction

High-strength low-alloy steels (HSLAs) play a significant role in critical structural components, due to their good combination of strength, fatigue resistance, toughness, ductility, and weldability. Their high strength-to-weight ratio enables their use in applications which require improved energy efficiency and benefit from reduced material volumes. Furthermore, compared with advanced composite materials,[1–6] the recyclability of HSLA steels offers a significant advantage. Often their unique properties are established in a well-designed thermomechanically controlled process, where grain refinement plays a crucial role in enhancing yield strength through the Hall–Petch effect,[7] which allows to simultaneously improve strength and toughness.

Precipitates formed by microalloying elements such as niobium (Nb) and titanium (Ti) as well as solute drag triggered by niobium segregation inhibit austenite grain growth and retard recrystallization, resulting in a refined ferritic matrix after phase transformation. In the present work, close attention is paid to niobium and titanium. By tying up carbon, niobium can also improve weldability. Titanium nitrides, on the other hand, reduce austenite grain growth during slab reheating. Due to their high solution temperature, they increase the toughness of heat-affected zones of welds.[8,9] However, larger particles can have a detrimental effect by acting as crack initiation sites. Therefore, a comprehensive understanding of the formation, evolution, and dissolution behavior of these precipitates is essential.

The presence of second-phase particles formed during aging[10] effectively increases the ultimate tensile strength. Advancements in transmission electron microscopy (TEM) and atom probe tomography (APT) paved the way for an in-depth analysis of chemical and physical particle properties, including the local chemical heterogeneity within the particles.[11–15] However, these techniques are time-consuming, expensive and, most importantly, only allow the examination of small material volumes, providing localized information and often suffer from poor statistics. To overcome this shortcoming, thermodynamic/kinetics simulations which capture overall tendencies while also rationalizing local experimental TEM and APT results are promising. These simulations are mainly based on thermodynamic mean-field calculations based on the CALPHAD method.[16–22] On their own, approaches involving Cellular automata,[23,24] Monte Carlo methods,[25] or Cluster dynamics[26] are less commonly used for the simulation of precipitation processes. Instead, these tools are more relevant for studying grain growth and recrystallization.

CALPHAD approaches rely on extremum principles. A critical issue with such models is their tendency to utilize the highest or

M. Laub, C. Motz
Chair for Material Science and Methods
Saarland University
66123 Saarbuecken Saarland, Germany
E-mail: motz@matsci.uni-sb.de

E. Detemple, S. Scholl
Research and Development - Products
AG der Dillinger Hüttenwerke
66763 Dillingen/Saar Saarland, Germany

The ORCID identification number(s) for the author(s) of this article can be found under https://doi.org/10.1002/adem.202500938.

DOI: 10.1002/adem.202500938

lowest local value of a specific property as the representative value. The composition of a precipitate is such a property. All simulation approaches have one feature in common: They minimize the Gibbs free energy (G) of the system, albeit in different ways. Related common concepts are *para*-equilibria, *ortho*-equilibria, and criteria addressing minimum energy barriers and maximum nucleation rates. The first two approaches generally assume that precipitates adopt the composition associated with the highest driving force ($\Delta G_{\max}$). Depending on the temperature, kinetics might be limited by diffusion. Therefore, contrary to the *ortho*-equilibrium, *para*-equilibrium calculations minimize G with respect only to fast diffusion elements. Minimum energy barrier approaches correct the driving force by accounting for a composition-dependent interfacial energy, which increases the growth rate of large particles on the expense of small ones. The last approach focuses on Gibbs enthalpy minimization by nucleation instead of growth; thus, the relevant composition is the one which yields the highest nucleation rate.

While all these approaches have their specific merits, they also have limitations. Limiting possible chemical compositions to just one without allowing for variations reduces the accuracy of the simulation. For example, using fixed extremum principles, does not allow to simulate the phase separation in the miscibility gap, which represents one of the key features of the Nb–Ti–C–N system.[27] Moreover, it is tedious to evaluate the turning points of higher dimensional functions because it requires the optimization of numerical methods and is associated with the need of high computational power.

In the present work, we combine the CALPHAD fundamentals with a Monte Carlo approach. This allows to simulate a dynamic range of particle compositions, resulting in a better representation of the compositional spreads compared to the mean-field models.

Table 1. Four experimental HSLAs with varying Nb and Ti levels in wt%.

Steel/composition	Nb	Ti	C	N	Mn + Si	Fe
3Nb-steel	0.030	0.005	0.10	0.0053	2.0	97.8
3NbTi-steel	0.030	0.026	0.12	0.0056	2.0	97.8
6Nb-steel	0.060	0.003	0.11	0.0050	2.0	97.8
6NbTi-steel	0.066	0.021	0.11	0.0056	2.0	97.8

2. Experimental Section

In the present study, four experimental HSLAs were investigated to provide reference data for modeling. Their chemical compositions are given in **Table 1**. The main interest of the present work was to explore the effect of Nb and Ti, which is reflected in the designations used for the four materials in Table 1. Two Nb levels (0.03 and 0.06 wt%) were considered (HSLAs: 3Nb-steel and 6Nb-steel). These Nb levels were combined with two Ti levels ($<$0.005 and 0.025 wt%), named 3NbTi-steel and 6NbTi-steel in Table 1. Notably, in all four HSLAs, manganese (Mn) and silicon (Si) levels were maintained constant at 1.7 and 0.3 wt%, respectively, and the C and N levels remained the same.

For all four HSLAs listed in Table 1, as-cast conditions and various heat-treated states were examined in cubic samples of $3 \times 3 \times 3\,\text{cm}^3$. Heat treatments involved temperature exposures at 1050, 1100, 1150, 1200, and 125 °C for holding periods of 10, 30, and 120 min, followed by quenching.

After processing, the samples were cut into halves. One half was used for the characterization of primary precipitates using optical microscopy (LOM) and scanning electron microscopy (SEM). The second part was used to prepare thin foils for TEM investigations of secondary precipitates and small pieces for wet chemical analysis to measure the amount of niobium and titanium in solution.

In the as cast state, the size distribution for primary precipitates was determined, distinguishing between titanium and nitrogen-rich primary TiN and niobium and carbon-rich primary NbC. Primary TiN particles could be directly observed on the polished surfaces using a Zeiss Axio Imager M light optical microscope, as shown in **Figure 1**d; the chemical composition was confirmed with energy-dispersive X-ray spectroscopy (EDS) measurements (Figure 1a–c). The TiN particles show a distinct gold-yellowish color. NbC particles, which exhibit the same color as the matrix in optical cross sections, were detected using a Zeiss Sigma VP SEM with back scatter electron (BSE) contrast (see **Figure 2**). Additionally, the phase fraction for primary TiN and NbC precipitates has been measured in all samples. The wet chemical analysis was done by dissolution of steel swarf in hydrochloric acid, filtration of the suspension and combustion analysis of the (Nb,Ti)(C,N) residues.

TEM was performed using a JEOL JEM2100 Plus, equipped with a LaB_6 gun operating at 200 kV. Chemical analysis of

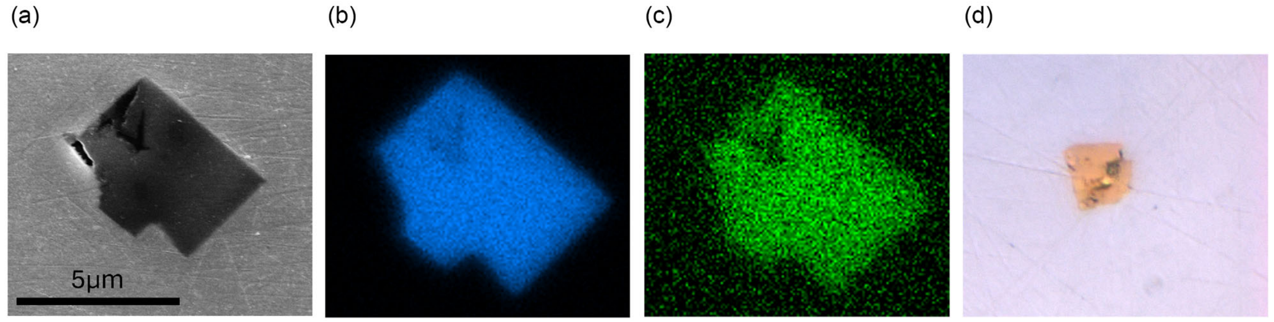

Figure 1. SEM image and Ti-N-EDS maps of primary TiN precipitates, LOM image of primary TiN: a) SE-SEM image, b) EDS Ti map, c) EDS N map, and d) LOM TiN.

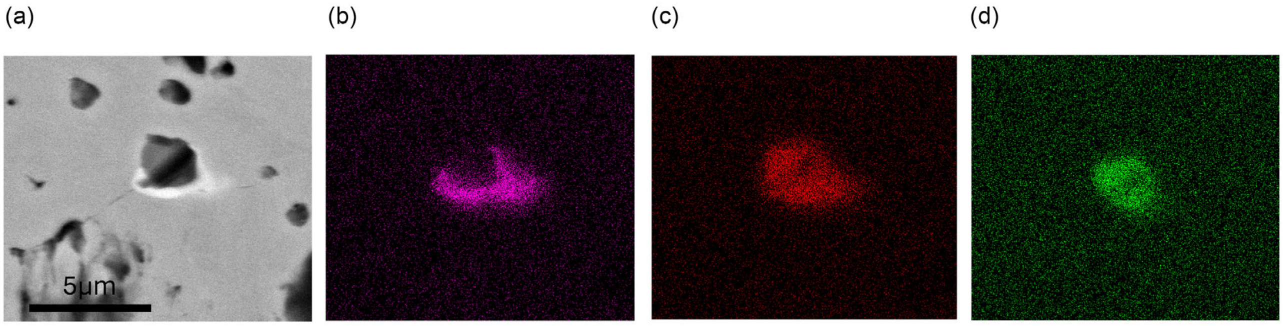

Figure 2. SEM image and Nb-Mn-S-EDS maps of primary-NbC, grown on top of a MnS precipitate: a) BSE-SEM image, b) EDS Nb map, c) EDS Mn map, and d) EDS S map.

(Nb,Ti)(C,N) precipitates was performed using EDS with a system from Oxford Instruments, as shown in **Figure 3**. Thin foils were prepared by grinding 3 mm diameter discs to a thickness of 50 µm, followed by twin-jet electropolishing in a TenuPol-5 (from Struers) to achieve electron-transparent foils with a thickness of no more than 200 nm. Good thinning conditions were achieved using an electrolyte consisting of 70 vol% methanol, 20 vol% glycerin, and 10 vol% perchloric acid, with flow rates between 15 and 20 and voltages of 30 ± 5 V at −13 ± 2 °C. From the four HSLAs in Table 1, a total of 32 TEM foils were investigated and a total number of more than 3000 particles were considered, which is about 94 particles per sample. For samples at lower heat treatment temperatures, this number is even higher whereas for samples at higher temperatures this number can be as low as 18 particles.

This similar particle analysis approach has been documented and applied in refs. [28,29]. The size distribution of (Nb,Ti)(C,N) precipitates was measured in the as cast state by dissolution of steel swarf in hydrochloric acid and scanning TEM of ultracentrifuged particle suspension.[30,31] This method has been used since the TEM-EDS analysis showed that many particles showing up in EDS mappings are invisible in TEM bright or dark field images and size measurements of particles from EDS mappings are too inaccurate.

3. Simulation Model

Precipitation models using the CALPHAD approach per definition assume that the system tends toward an equilibrium state. While this state is the most stable from a thermodynamic point of view, it can be observed very rarely, especially when it's about kinetics. The major drawback is the implementation of the mean-field theory, which attempts to approximate multiple degrees of freedom by averaging them into effective mean values. The present model aims to minimize this error, inherent to mean-field approximations, by considering the distribution with a particular focus on the composition distribution. In the current model, nucleus compositions are not restricted to only one composition, but can occupy the whole compositional space between Nb–Ti and N–C. During the subsequent kinetic processes, these compositions can change. To cover the kinetics of the change in compositional distribution, the direction of compositional change is coupled to the local gradient of the composition-dependent chemical driving force, which is implemented through a Monte Carlo approach. The change in composition is therefore given by a probability that considers the possible change in free energy due to the change in composition with respect to the thermal energy of the system. The kinetics of this transition is determined by diffusion. For this purpose, Fick's second law for radial diffusion in 1D is implemented. Within the CALPHAD system,

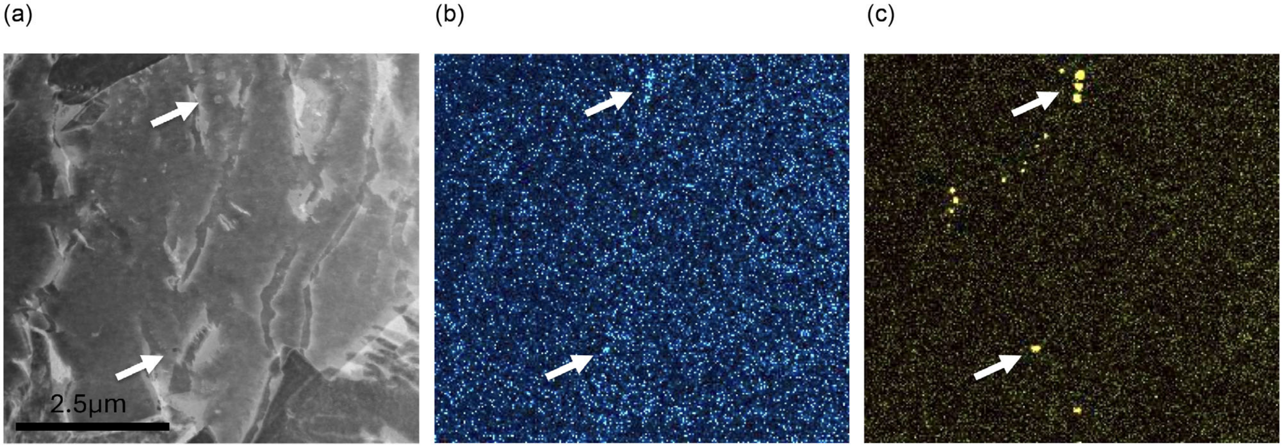

Figure 3. STEM image and Nb-Ti-EDS maps of secondary NbTiCN precipitates: a) STEM image, b) EDS Nb map, and c) EDS Ti map.

elements occupying different sublattices are treated independently. However, for species on the same sublattice, the diffusion rate is determined by the species with the lowest diffusion, as it limits the overall diffusion process.

3.1. Introduction of Precipitation Populations

The continuous change in composition, in addition to the change in size, makes it inefficient to categorize precipitates solely based on size, since particles within the same size class may have different compositions and, therefore, different driving forces. Consequently, particles must be categorized according to size and composition. This results in a so-called "population," in which particles of same size and same composition are handled. Populations can change continuously in size and composition, however, the number of particles within a population always remains the same. Since the probability of two populations having the same size and composition is extremely low, merging of populations is not implemented. The resulting error, even if it is small, from merging of two populations outweighs the minor computational benefits of population reduction. The parameters which define a population class are listed in **Table 2**.

The equilibrium composition c^{eq} is defined as the composition on the outer shell of the particle. It is decisive for the determination of the driving force of the considered population class. At the same time, it is the composition that the population class strives for. The mean composition $\tilde{c}$ can be calculated by numerical integration of the composition profile c along the radius. The composition profile c of the population class is an array representing the calculated concentration profile of each element along the radius at distinctive grid points. The last entry value of the composition array is the composition at the outer shell, c^{eq}. The lateral resolution holds the information of the spacing of the grid points, δr. The class volume ν^{pop}, which represents the phase fraction of the population class when normalized to the simulation volume of one mole, is required, together with $\tilde{c}$, to calculate the precipitated amount of each element within the population class. The calculation of N and the kinetic equations governing size can be found in the Appendix A. The definition of a population class is visually represented in **Figure 4**.

Table 2. Parameters identifying a precipitation population.

Parameter	Abbreviation
Number of particles in the population	N
Radius	r
Equilibrium composition	c^{eq}
Mean composition	$\tilde{c}$
Composition	c
Lateral resolution	δr
Population volume	ν^{pop}

3.2. Composition Evolution

Regarding the compositional evolution of the population classes, three assumptions are made: 1) The outer shell of a particle is always in equilibrium with the surrounding matrix. 2) Exchange of matter is based on diffusion, given by Fick's second law. 3) The probability of a population class to adopt a certain equilibrium composition c^{eq} is calculated based on the gradient of the driving force at the current equilibrium composition relative to the thermal energy of the system.

The equilibrium composition that every particle tries to attain is calculated in every iteration by an Arrhenius evaluation of the driving forces of the neighboring compositions of the current equilibrium composition c^{eq} (see **Figure 5** and Equation (1)). The formalism for the kinetic evolution has been adopted.[16,17]

The probability P of a population class with current driving force F_0, according to its current equilibrium composition c^{eq}, to change its equilibrium composition by an increment δc to $i = c_{\mathrm{sublattice1}} \pm \delta c$ and $j = c_{\mathrm{sublattice2}} \pm \delta c$ is given by

$$P_{i,j} = \frac{\exp\left(\frac{F_{i,j} - F_0}{\mathrm{RT}}\right)}{\sum_{m=-1}^{1} \sum_{n=-1}^{1} \exp\left(\frac{F_{i+m,j+n} - F_0}{\mathrm{RT}}\right)} \tag{1}$$

in which F_0 is the driving force corresponding to c^{eq}, $F_{i,j}$ is the driving force of the neighboring compositions of c^{eq}, R is the gas constant, and T is the temperature in Kelvin. The evaluation of the driving force is also given in the Appendix A. Based on the probability $P_{i,j}$, the new equilibrium composition is chosen. Compositions with a higher driving force than the current c^{eq} have a higher probability to be selected as new c^{eq} than compositions with lower driving forces. At higher temperatures, the

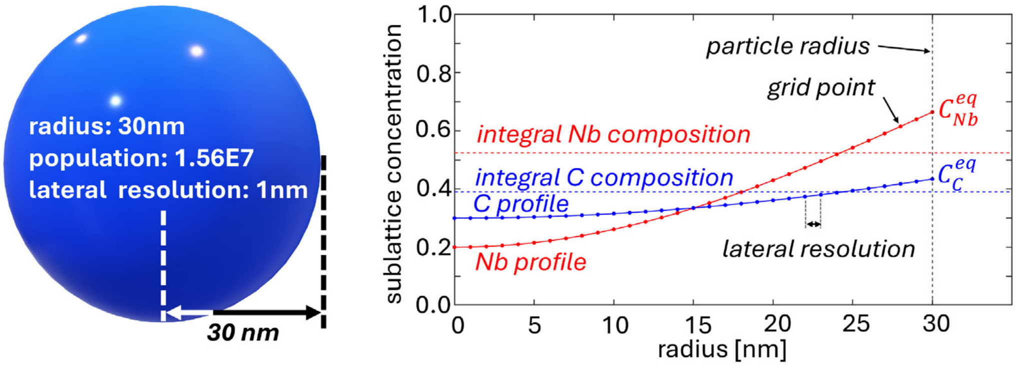

Figure 4. Parameters of a precipitation population class.

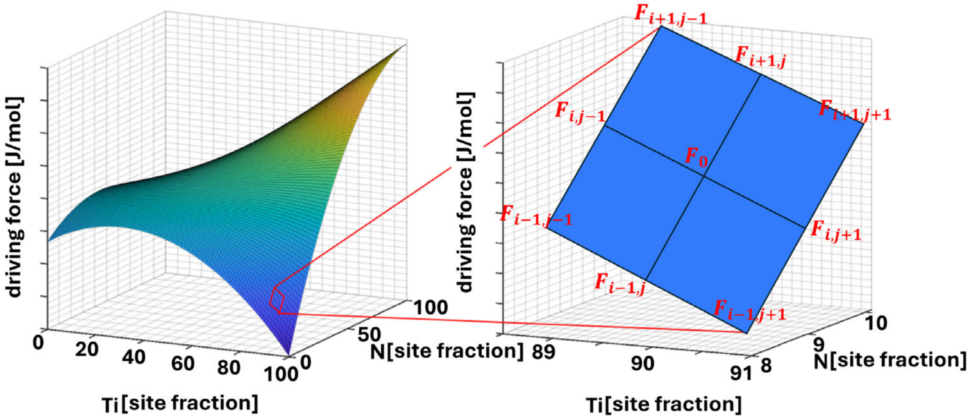

Figure 5. Left: Composition-dependent driving forces and right: enlarged section of the driving force surface with marked driving forces of the neighboring compositions of c^{eq}.

difference in probabilities between high and low driving forces is reduced, due to the increased thermal energy in the system. Therefore, coupling the equilibrium composition to the local gradient leads to an equilibrium composition that tends toward the composition with the highest driving force. This can be a local or global maximum. If the equilibrium composition is at a local maximum, the thermal energy RT and the depth of the miscibility gap determine whether it is beneficial to stay with the composition in the local maximum as metastable or to transition through the miscibility gap toward the composition in the global maximum. The change in composition is based on a simple diffusion model, treating precipitates as spherical objects with isotropic diffusion in radial direction. The diffusion equation for this mechanism is therefore assumed to be Fick's second law for spherical objects:

$$\frac{\partial c}{\partial t} = \frac{\partial^2 c}{\partial r^2} + \frac{2D}{R}\frac{\partial c}{\partial r} \tag{2}$$

with the concentration c, time t, radius r, and diffusion constant D. The side conditions are $\frac{\partial c(r=0)}{\partial r} = 0$ for reasons of symmetry and $c(r = R) = c^{\mathrm{eq}}$. The diffusion equations for each particle population are solved by the highly optimized Crank–Nicolson method[32]:

$$\overline{\mathbf{A}}\bar{c}_{t+dt} = \overline{\mathbf{B}}\bar{c}_t \tag{3}$$

with $\bar{c}_t$ being the known concentration at time t of the desired element at known grid points and $\bar{c}_{t+dt}$ the unknown concentration at time $t + dt$. This equation is solved independently for each sublattice. In the present case, where each sublattice is limited to only two species, the diffusion equations problem can be reduced to one diffusion equation per sublattice. The concentration gradient of the left out element can be calculated as remainder top unity. It is assumed that, for each sublattice, the rate limiting species determining the exchange of matter, is the one with the smaller diffusion coefficient, since particles cannot enrich faster with one element than they can deplete on the other element, without growing. Therefore, Equation (3) always solves for the concentration profile of the slower diffusing species. The diffusion coefficients for diffusion within the particles are based on a CALPHAD approach and therefore depending on temperature and composition itself. The concentration profile of the faster diffusing species is given by the difference to unity. The first boundary condition of zero concentration gradient at the core of the precipitate $\frac{\partial c(r=0)}{\partial r} = 0$ is implemented using second-order accuracy backward finite difference coefficients. This discretization scheme necessitates three grid points to work. Consequently, the method for simulating matter exchange by diffusion can only be applied to particles encompassing at least four grid points. In simpler terms, the radius must be at least 4 times larger than the lateral resolution of the grid. For particles smaller than this threshold, the change in composition is assumed to be instantaneous. Considering a default lateral resolution of 1 nm and the limited change of c^{eq} to the neighbor compositions, this assumption seems to be a reasonable simplification for smaller particles. The change of composition of the size increment on the most outer shell of the particle, $R - \mathrm{floor}\left(\frac{R}{dr}\right) \cdot dr$, smaller than the lateral resolution, cannot be calculated by diffusion. It is instead assumed that the outermost shell composition is the same as the composition at the last grid point, namely c^{eq}, as shown in **Figure 6**.

Because the equilibrium compositions that each population class tries to achieve are randomly chosen based on their probability, it is therefore theoretically possible for specific classes to dominate the overall kinetic behavior. For instance, a population class consisting of many large particles might continually attempt to adopt compositions that result in a lower or even negative driving force, leading to the slow dissolution of these particles. Conversely, small particles could enrich in some elements faster compared to a scenario with fewer but larger particles of the same overall phase fraction. These contrasting events would result in totally different outcomes. To prevent a single population class from dominating the overall kinetics, population classes with a relative phase fraction larger than 1‰ are subdivided. This is achieved by creating a clone of the affected population class and halving the population in each of them. Both newly formed population classes are subsequently treated independently, each taking their own path according to Equation (1).

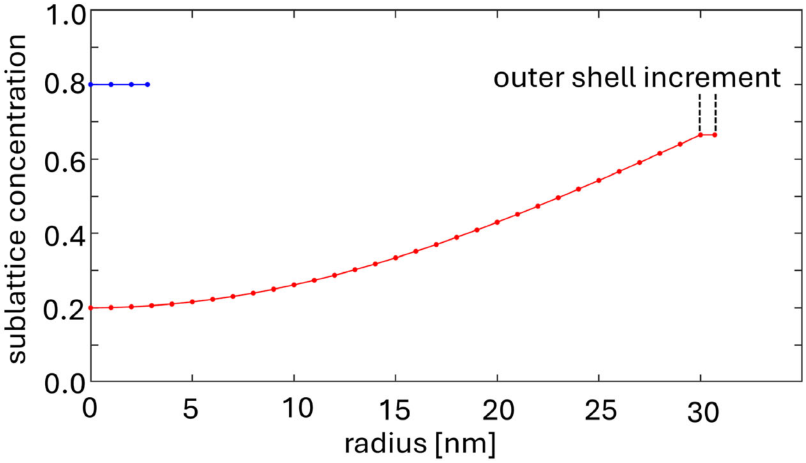

Figure 6. Schematic concentration profiles: a particle larger than 4 · dr (red) and a particle smaller than 4 · dr (blue).

3.3. Nuclei Composition

Contrary to most commonly used extremum principles, all compositions that result in a positive driving force are allowed as nuclei composition. The exact composition initialized is random. This way each composition has the same probability, but the initialized population class will differ in the amount of particles N, based on the nucleation rate, and in the size of the particles, based on the critical radius. Furthermore, the number of different population classes will be initialized at once per discrete timestep. The maximum number should be kept as low as possible to reduce calculation time, but must be high enough to cover the profile of the composition-dependent nucleation rate. A number of 25 population classes has been chosen for this purpose, satisfying both conditions. **Figure 7** shows an example image of nuclei with different compositions initialized with a population proportional to their nucleation rate. The nucleation model used is described in greater detail within the Appendix A. It is based on the classical nucleation theory (CNT) and does only consider homogeneous and heterogeneous nucleation at dislocations. It does not incorporate more realistic scenarios as nucleation during fcc–bcc phase transformation or precursor nucleation.

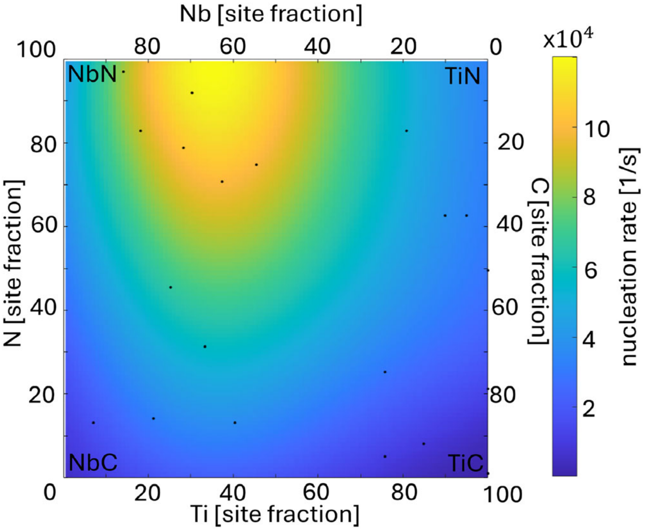

Figure 7. Composition-dependent nucleation rate; compositions at which population classes are initialized are marked with black points.

4. Results and Discussion

Unfortunately, no literature has been found that deals with the compositional distribution of Nb/Ti carbonitrides within HSLA steels in great detail, neither measurements nor simulations. Most publications only present mean values of the measured data or grade the particles according to their dominant anions.[12,13,33,34] Most of the time, precipitation compositions are assumed to be stoichiometric[35] or at equilibrium composition, either calculated using a thermodynamic approach[16,36,37] or based on solubility products.[21,27] Only studies by Dijk et al.[38] and Craven et al.[8] showed the spread in composition for a handful of particles. Deschamps and Hutchinson[39] discussed the fact that the assumption of a constant composition throughout the precipitation process is a bad approximation and that neglecting nonstoichiometric and nonequilibrium compositions, supported by differences in solute diffusivities and segregations, may lead to an underestimation of the nucleation rate. Additionally, the wide range of possible C/N ratios and the miscibility gap within the Nb/Ti system make the use of the compound energy formalism within computational thermodynamics superior compared to the use of solubility products. Also, Costa e Silva[40] emphasizes the importance of composition-dependent interfacial energies and their effect on the kinetics of nucleation, phase fraction, and particle size. Unfortunately, the capability of current modeling approaches does not cover these crucial features to their full extent.

The presented model successfully captures the kinetic and the transition of the compositional distribution from stable particles around a local equilibrium, through the miscibility gap of metastable particles, to particle composition distributions spreading around the global equilibrium composition. **Figure 8** depicts a snapshot showing the transition of the initial particle

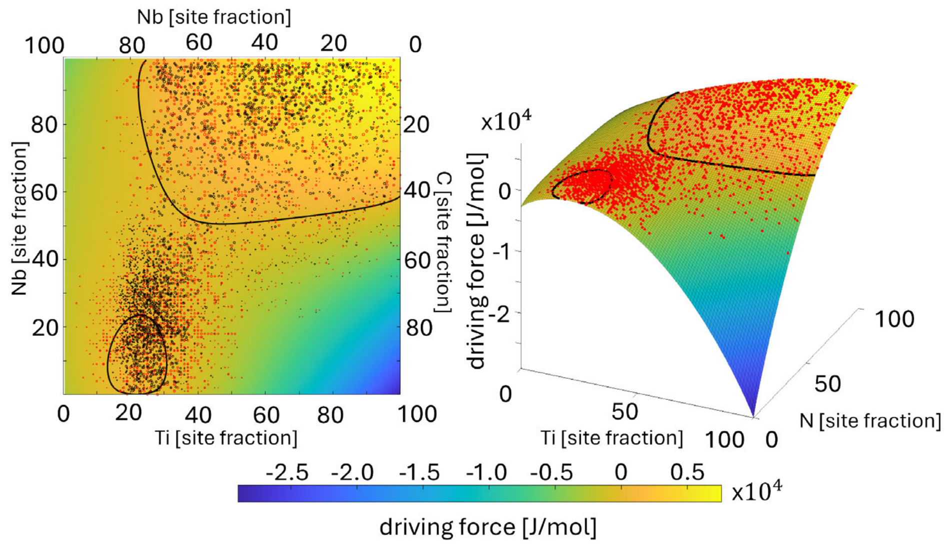

Figure 8. Example images for the 3Nb-steel at 115 °C, left: top view on composition dependent driving force with integral particle compositions (black points) of the populations and corresponding equilibrium compositions (red points) of the populations, the black line represents the zero driving force iso-line, right: side view on composition dependent driving force with only equilibrium compositions (red points) and zero driving force iso-line.

composition of the 3Nb-steel (around a $Nb_{80}Ti_{20}C_{90}N_{10}$-composition, as shown in Figure 11a) evolving toward the most stable composition in the titanium- and nitrogen-rich region. It is also evident that new particles have formed spaciously within that region. Also, within the miscibility gap, nucleation of precipitates takes place, but they start to enrich with niobium or titanium to stabilize. In the illustrated case, due to the high temperature, the compositions within the miscibility gap have a negative driving force, leading to the dissolution of small particles while larger ones reach stable compositions before dissolving. Consequently, the particle distribution is separated into two distinct populations: initial particles that change their composition toward more stable ones, and newly formed particle populations which may dissolve over time, particularly for compositions with a highly negative driving force (e.g., TiC). In contrast, populations with a less negative driving force (e.g., NbN) might persist and eventually achieve stability through further enrichment with titanium. As aforementioned, the nucleation model lacks advanced nucleation mechanisms, probably leading to an underestimation of the nucleation rate. This is due to the fact that the main focus of the proposed model is the description of the transition and evolution of already existing particles, rather than a more accurate nucleation rate. It is assumed that this inaccuracy has only little impact on the overall results, since all precipitates, either formed during solidification or phase transformation are included in the precipitation distribution of the starting conditions. This reduces the error of the nucleation model of the limited time during the ramp up phase of the heat treatment.

The process of enrichment, as well as the dependency of size and composition or the change in composition over time, is shown in **Figure 9**. Several effects are displayed: In subfigure 9a the concentration profile of 10 randomly selected populations

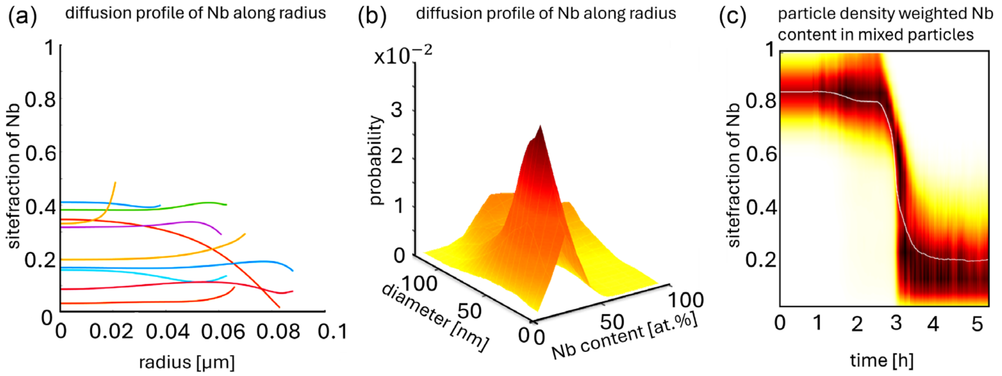

Figure 9. a) Nb concentration profiles along the radius of 10 randomly selected population classes. b) Size-dependent composition histogram with the majority of smaller, low Nb particles and a second, half hidden peak for larger particles with a higher Nb concentration. c) Color coded histogram (probability of particle composition increasing from white over yellow-orange-red to black) of particle Nb concentration over time for the 125 °C isothermal heat treatment given in Figure 10a, shifting from Nb-rich at the beginning to Ti-rich at the end, white line represents mean site fraction of Nb.

from Figure 8 can be seen. While most of the concentration profile show a steady trend, two of them stick out. One profile shows a steep increase in Nb concentration, indicating a core shell configuration of a small particle near the local equilibrium composition in the Nb/C-rich corner, the other profile shows a continuous decrease in Nb reaching almost pure Ti at the outer shell, larger particles enriching with titanium on their way to the global equilibrium. In subfigure 9b two distinct population clusters, corresponding to the local and global equilibrium composition, can be observed. The population in front with the higher probability consists of particles with a Nb concentration of less than 50 at% and a size up to 50 nm, whereas the second population, which has a higher Nb concentration and also larger in size is hiding behind the first one. These two populations correspond to newly formed Ti-rich particles that have formed during the annealing and to the initial particles, formed during cooling after casting, that are currently in a transitional state from their initial composition toward a Ti-rich composition. Unlike subfigure 9a and b, which are only a snapshot in time, subfigure 9c shows the development of the particle composition during the kinetics. While at the start, the particle Nb concentration scatters around the initial particle composition ($Nb_{80}Ti_{20}C_{90}N_{10}$), a change in composition can be seen during heating. Surprisingly, even though the most stable particle composition (according to the driving force in Figure 8a) is very close to a pure TiN (bright yellow region), the majority of the particles in the simulation as well as in measurements (comparison of most stable compositions in Figure 8 and the 125 °C 30 min treatments in Figure 11) do not attain this composition, but scatter around the composition corresponding to the turning point in the driving force, meaning that for the given thermal energy of the system and the given driving forces at these compositions, the probability of enrichment is the same as for the impoverishment. This can be interpreted as that the additional gain in free energy by a compositional change toward a stoichiometric TiN composition might be too small compared to the thermal energy of the system at a given temperature. It is also possible that these particles are stabilized by entropy effects, meaning that the gain in enthalpy

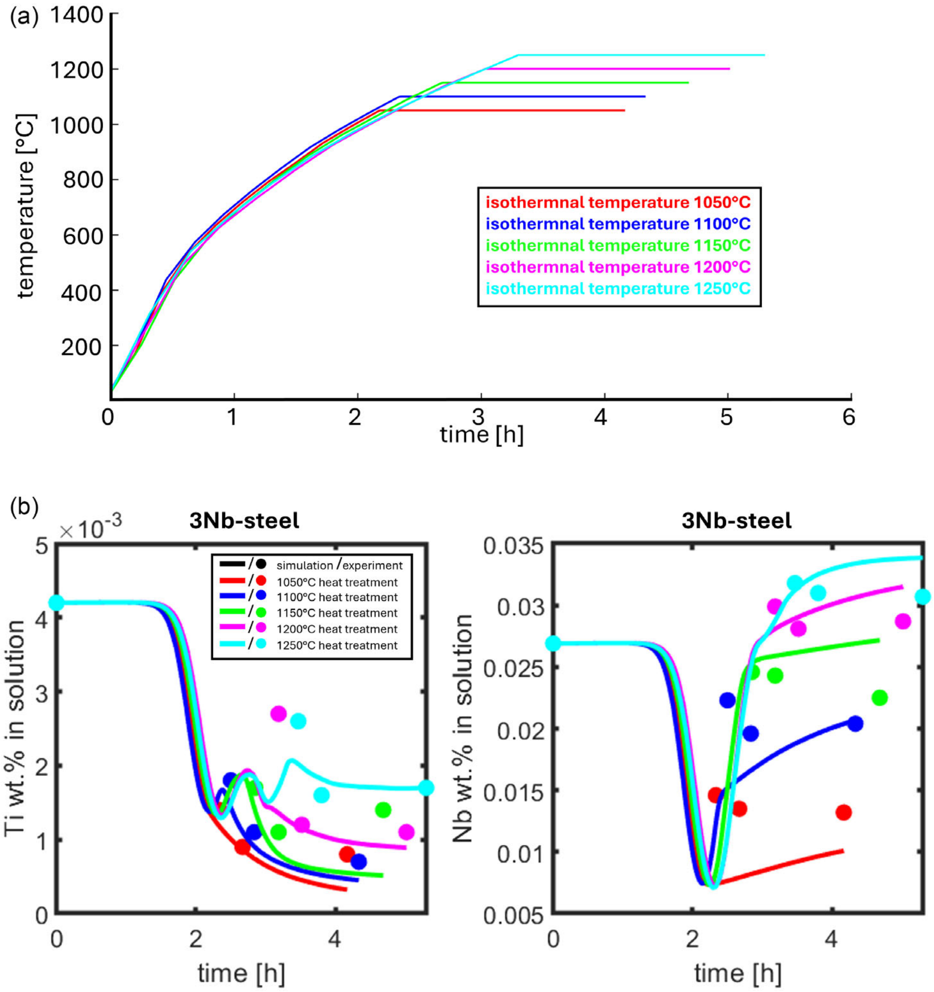

Figure 10. a) Temperature profiles of the different heat treatments. b–e) Ti and Nb content in solution for the different steels, color coding according to (a), simulation results in solid lines, wet chemical measurements marked as dots.

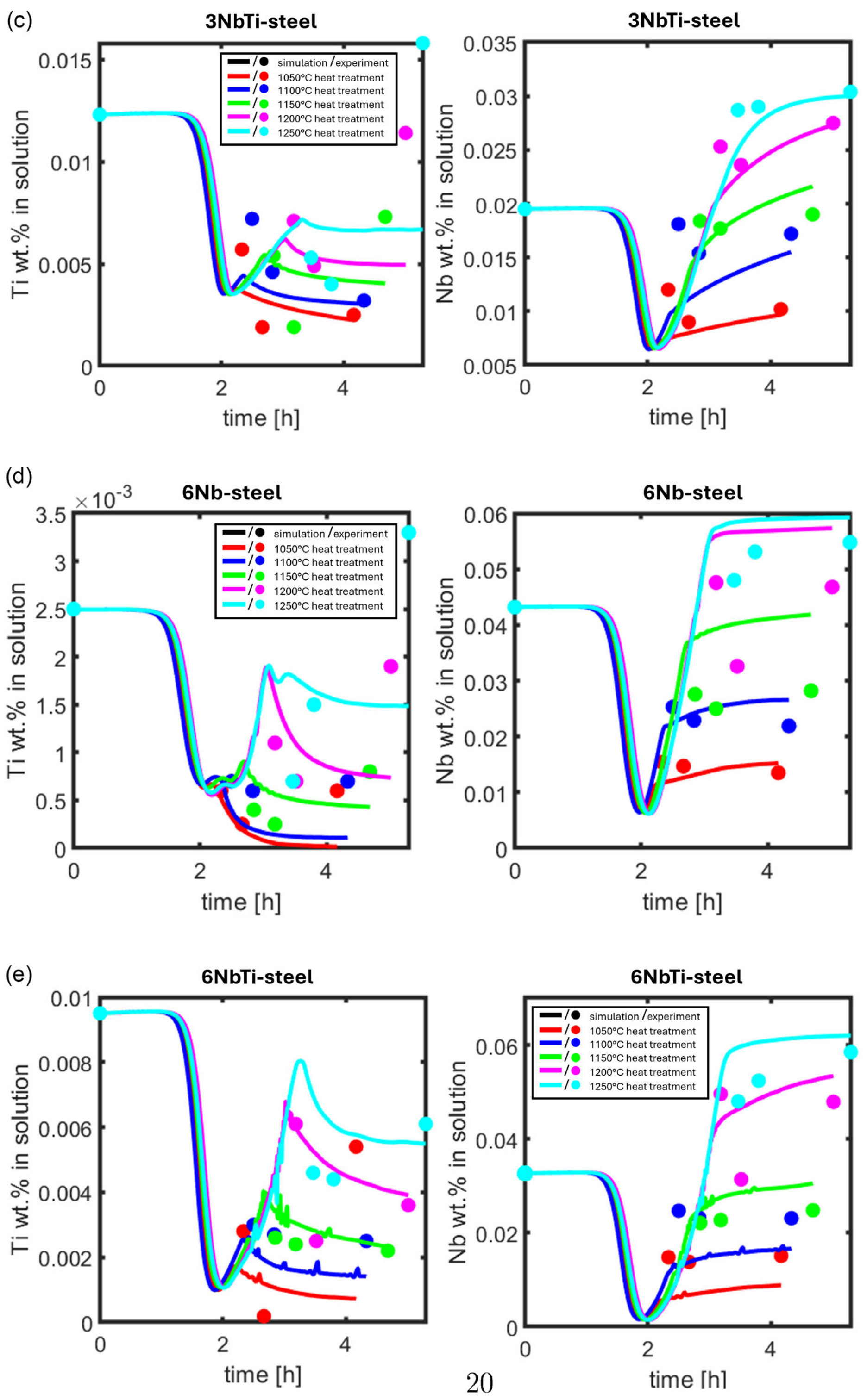

Figure 10. Continued.

by further enrichment with Ti, especially at high temperatures, is less than the gain in entropy that comes from the minor Nb concentration. This results in a lower Ti concentration within the particles in comparison to equilibrium calculations and therefore an increased Ti concentration within the matrix, as one might expect, according to extremum principle calculations.

4.1. Experimental Validation of the Model

The overall behavior of all precipitated phases is hard to quantify. Direct observation of the growth, nucleation and dissolution is impossible, but some properties can give a hint about the ongoing kinetics. For this purpose, the niobium and titanium content in solution have been measured and have been compared to the values of the simulation, as presented in **Figure 10**b–e. As can be seen, the amount of Nb and Ti in solution has the same tendency and order of magnitude when comparing measurements with simulation. In some cases, the simulation is more or less on spot with the measured data, but most of the time, the deviation from simulation to measurements is about 10–50%. All data and simulations follow the tendency to first decrease the amount in solution, sometimes followed by an increase, depending on the heat treatment. This can be traced back to the precipitation of particles during the heating up phase, followed by a dissolution at higher temperatures. Regarding the Ti content in solution, the data from the wet chemical analysis scatter way more than the data for the Nb content. This is due to the lower Ti content compared to niobium, especially for the Ti-free steels, in the first place and founded in the resolution limit of Ti with this method, leading to an uncertainty way larger than the influence of temperature for the different heat treatments. For Nb, the picture is much clearer, showing explicit difference for the different temperatures in the simulation as well as for the measured data. In all cases, it is important to take the influence of primary

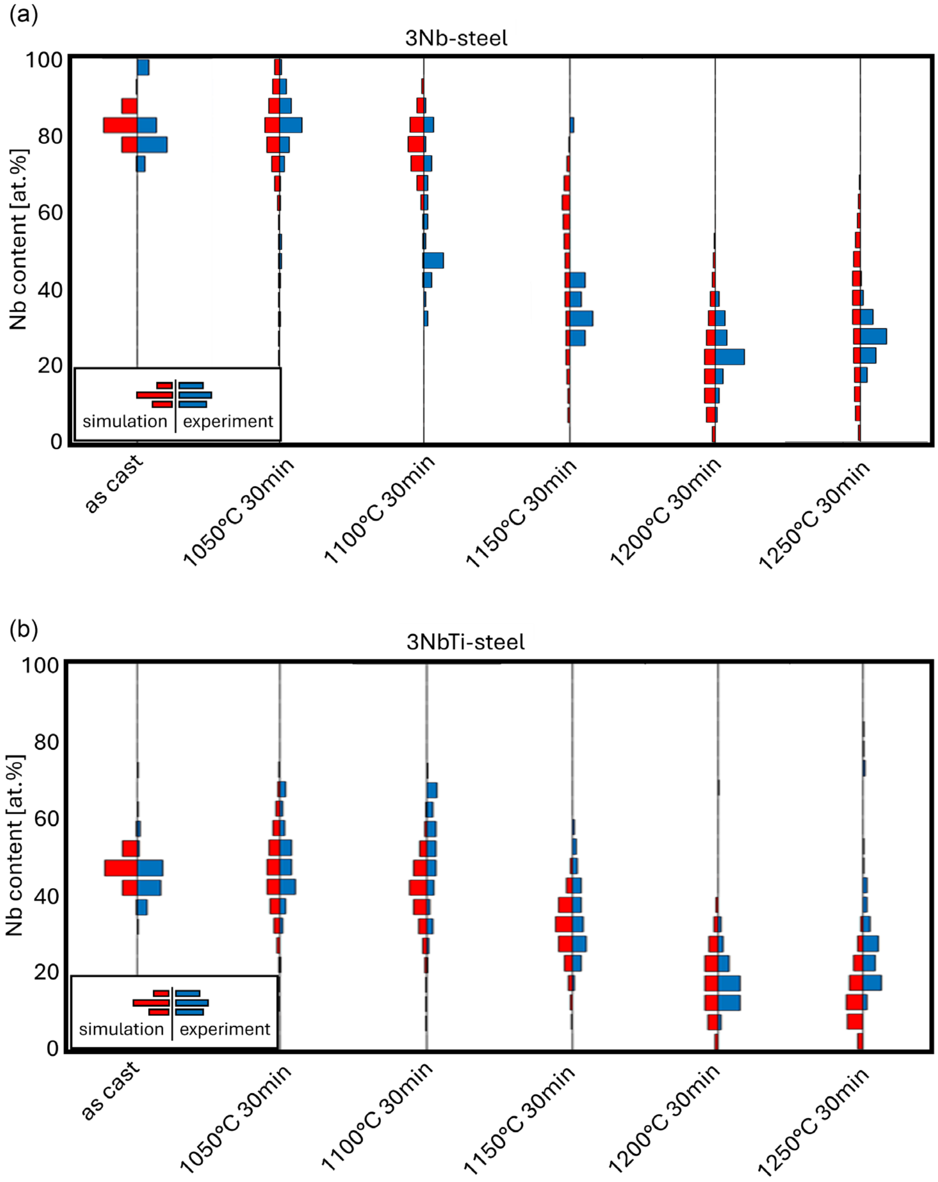

Figure 11. Comparative histograms of measured particles composition in blue and simulated particles compositions in red. All histograms are normalized to the same height for better comparison of the Nb content of the main lattice of precipitates within the steels: a) 3Nb-steel, b) 3NbTi-steel, c) 6Nb-steel, and d) 6NbTi-steel.

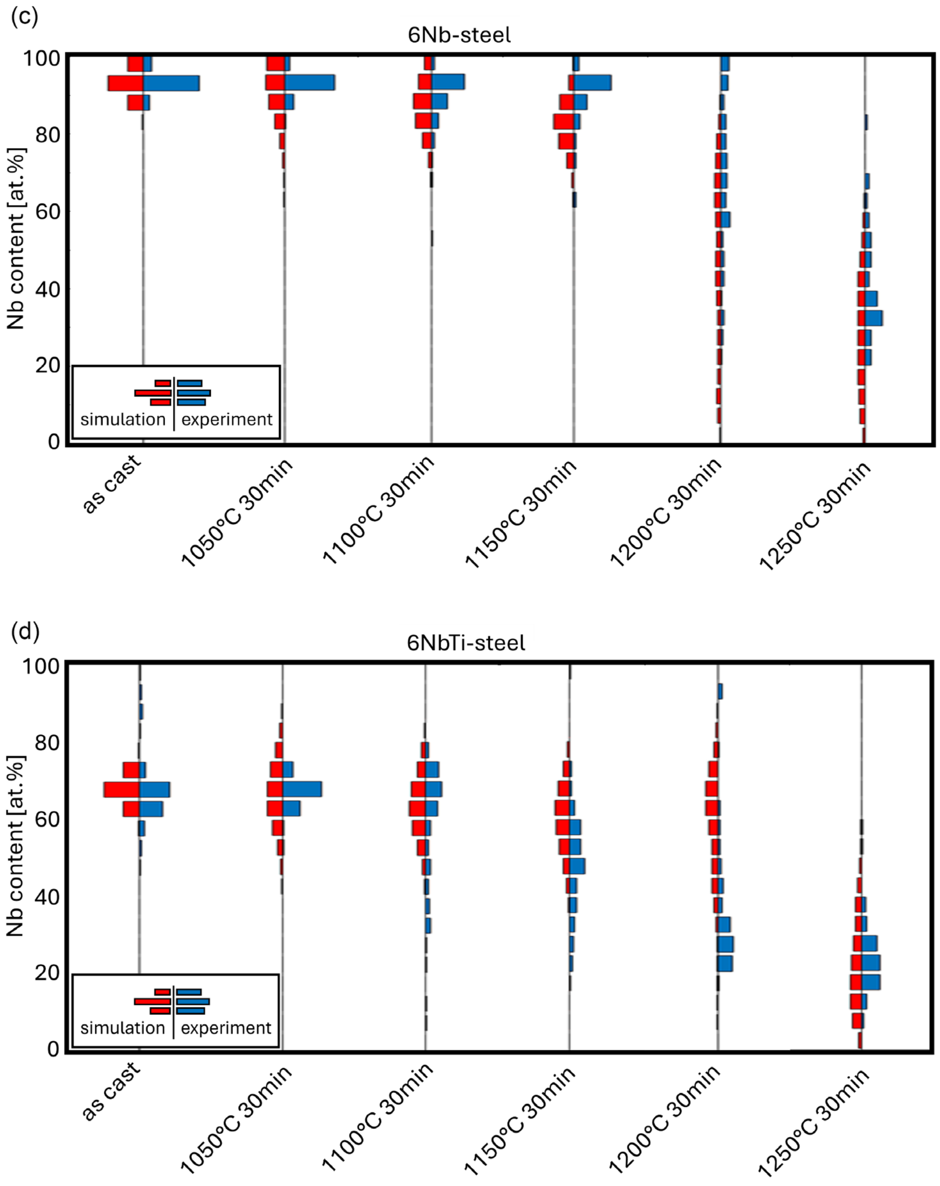

Figure 11. Continued.

precipitations into account. Contrary to small secondary precipitates, which will rapidly dissolve at given temperatures, primary precipitates can tie up large amounts of Ti and Nb, that will, if at all, only very slowly go back into solution at the used heat treatments. Therefore, the phase fraction of these particles must not be neglected when setting up the initial conditions for the simulation. Phase fractions in the range of $3 \cdot 10^{-4}$ up to $6 \cdot 10^{-4}$ as measured for primary TiN in the Ti containing steels, can tie up to 50% of the overall Ti within the steel, 50% of Ti that is bound in the long term and cannot contribute to any future nucleation of fine dispersed, effectively pinning, secondary precipitates.

The simulated particle compositions were validated against experimental data. The particle compositions of the samples listed in Section 2 were compared to the integral particle compositions from the simulation at the same conditions. It should be mentioned that the simulated precipitates consist of Nb, Ti, C, and N, but quantification of C in EDS is in general problematic. Therefore, carbon was excluded from all the quantification results of the obtained particle spectra. In the following approach, the contents of Nb and Ti in the particles are normalized and the relative Nb (at%) is calculated by the following equation:

$$\text{rel. Nb(at\%)} = \frac{\text{Nbat\%}_{\text{EDS/simulation}}}{\text{Nbat\%}_{\text{EDS/simulation}} + \text{Tiat\%}_{\text{EDS/simulation}}} \times 100\% \tag{4}$$

It can be seen from **Figure 11** that all simulated results show rather good agreement with the experimental results. As expected, at high temperatures, only titanium-rich compositions

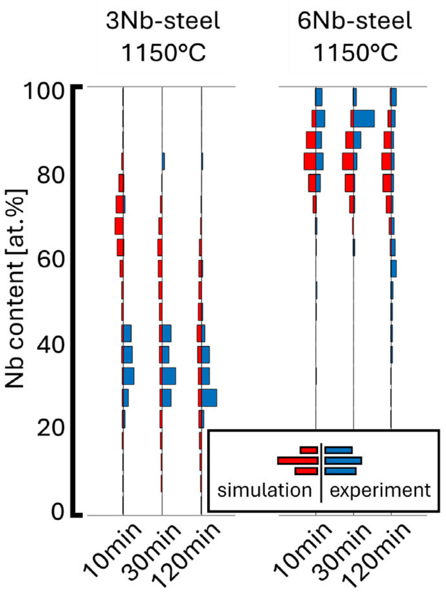

Figure 12. Detailed view of Figure 11b,d for 115 °C heat treatment showing measured and simulated particle composition evolution over time. Measured particles in blue and simulated particles in red.

are stable, whereas depending on the steel composition, particles with a higher niobium content can be found at lower temperatures. A closer look at the change in particle composition in time is shown in **Figure 12**. For the two Ti-free steels, the particle composition has been measured at three points in time for the 115 °C isothermal heat treatment. It is evident that for the majority of the measurements, the simulated particle composition spectrum is wider than the corresponding measured particle compositions. It can be also seen, that for both steels, even though the particle compositions of the simulation represent the measured values quite well, the simulation seems to be lagging behind regarding the kinetics of the change in composition. A significant benefit of this approach is its ability to assign unique compositions and kinetic profiles to each population. This aligns well with the principles of statistical thermodynamics and offers a more realistic representation compared to models where all particles exhibit identical behavior. The implementation of a full diffusion model offers a substantial benefit by enabling time-dependent compositional changes. In contrast, traditional models assume instantaneous adoption of equilibrium concentration by particles. This combined approach, along with the calculation of probability-driven kinetic pathways for each population class, allows for highly accurate simulations of particle composition transitions. Notably, the model can capture the transformation of Nb-rich particles to Ti-rich particles through the miscibility gap. The unique capabilities of this CALPHAD-based approach combine the advantage of a very accurate particle composition distribution as well as the temporal resolution of transition states. At the same time, the possibility to check for size-dependent compositions or even compositional changes along the radius paves the way for many interesting topics, such as process conditions for multimodal compositional particle distributions or the formation of core-shell particle configurations.

While diffusion is undeniably the primary mechanism responsible for compositional changes in particles, solving Fick's second law remains a hurdle that some researchers rather bypass for the sake of performance.[41] The proposed method effectively reduces the number of diffusion equations that are necessary to solve to $n-1$, where n is the number of species per sublattice. This approach demonstrates promising results and yields accurate precipitation composition predictions for four-component precipitates. Although solving diffusion equations requires substantial computational time, the assumptions made in this model allow for a significant reduction in computational cost. By solving only the two necessary equations, the time required for simulations is greatly reduced. In the code used for the current study, computational time could be reduced to as little as 300 s on a workstation depending on the specific heat treatment, which is very fast compared to other methods and represents a minimal investment considering the added value of the results.

5. Conclusion

Multiscale characterization of the precipitation status of Nb–Ti microalloyed HSLA-steels was performed. Due to the tremendous amount of analyzed particles, the behavior of the composition spectrum of carbonitride precipitates could be investigated with unprecedented accuracy in terms of compositional and temporal resolution.

State-of-the-art computational thermodynamic simulations based on extremum principles are not capable of covering the presented behavior, leading to deviations because of the neglection of the underlying characteristics of the compositional distribution.

The presented model aims to compensate for these disadvantages by allowing different compositions, managing their enrichment and depletion behavior by a probabilistic Monte Carlo approach. This unique combination of CALPHAD and Monte Carlo simulations enables the model to reproduce the measured behavior and reveal the underlying effects.

The data in correlation with the simulation lead to the conclusion that in the thermodynamic system of Nb/Ti carbonitrides, two precipitation clusters, on one hand the niobium/carbon-rich particles, on the other hand the titanium/nitrogen-rich particles coexist most of the time. Nucleation can take place in both regions, and a transition of particles between both equilibrium compositions can appear.

This study shows that the kinetics of the transition of particles between the local and the global equilibrium composition though the miscibility gap of the Nb/Ti system can be accurately simulated by a simple 1D radial diffusion model.

Primary TiN forming during solidification are small in quantity but can have a high phase fraction. These particles must be included within the simulation even if their behavior is not of primary interest, as they can tie up large amounts of Ti and N which will not be available for growth and nucleation of process relevant secondary precipitates, as primary TiN do not dissolve over time, even at high temperatures.

Appendix A

Following the equation for the calculation of driving forces, critical radii and nucleation rates are given for completion. They are taken from refs. [16,17,42,43].

The driving force can be divided into a chemical component λ_c and into a mechanical component λ_m. The chemical component is based on the difference in chemical potentials of the participating elements in the precipitation phase and the matrix. The mechanical component is associated with misfit strains at the interface and is therefore dependent on the misfit of the lattice constants and mechanical properties of the precipitation phase and the matrix.

$$F = -\lambda_c - \lambda_m \tag{A1}$$

λ_c is given as

$$\lambda_c = \sum_{i=1}^{n} c_i^p \left(\mu_i^p - \mu_i^0\right) \tag{A2}$$

with c_i^p being the concentration in mole fraction of element i in precipitation phase p, μ_i^p as the chemical potential of element i in precipitation phase p, and μ_i^0 as the chemical potential of element i in the matrix. The mechanical component λ_m is given by

$$\lambda_m = \frac{3}{N}\varepsilon^2 E_0 \tag{A3}$$

with

$$N = (1+\nu_0)\frac{E_p}{E_0} + 2\left(1 - 2\nu_p\right) \tag{A4}$$

and

$$\varepsilon = \frac{1}{3}\frac{\sqrt{2}a_0 - a_p}{\sqrt{2}a_0} \tag{A5}$$

here, E_p and E_0 are the Young's modulus of the precipitating phase and the matrix and ν_p and ν_0 the Poisson ratios of the precipitation phase and the matrix. a_p and a_0 are the lattice constants of the precipitating phase and the matrix. The value of $\sqrt{2}$ corrects the misfit ε for the Nutting–Baker orientation relation. Note that the values of E_p, ν_p, and a_p can be dependent on composition.

The interfacial energy γ between precipitation phase and matrix can be estimated by the enthalpy of solution ΔH_{sol}.

$$\gamma = \frac{n_s Z_s}{n_L Z_L}\Delta H_{\text{sol}} \tag{A6}$$

n_s, Z_s, n_L, and Z_L are values depending on the crystal structure of the matrix, of the interface and on the molar volume of the precipitation phase. The molar volume of the precipitation phase can be expressed in terms of the lattice constant a_p. These values are not independent in reality, as they differ depending on misorientation between matrix and precipitate. Since no preferential misorientation for different types of precipitates is known and the misorientation would additionally change with grain boundaries moving across particles, a more pragmatic approach is chosen. For a [100] interface in an face centered cubic (FCC) matrix, a mean value, averaged over all matrix-precipitate misorientations, can be given as

$$K = \frac{n_s Z_s}{n_L Z_L} = 0.329\frac{\left(\frac{4^{\frac{2}{3}}}{a_p^2}\right)}{N_A} \tag{A7}$$

where N_A is the Avogadro constant. Therefore, γ can be written as

$$\gamma = K\Delta H_{\text{sol}} = K\lim_{f_p \to 0}\frac{\partial H_0}{\partial f_p} \tag{A8}$$

with H_0 as enthalpy of the matrix and f_p as the phase fraction of the precipitation phase.

The enthalpy as well as the chemical potentials can be extracted from the Gibbs free energy, provided by the CALPHAD approach (see Appendix B).

The energy barrier for nucleation ΔG can then be evaluated as

$$\Delta G = f\frac{\gamma^3}{F^2} \tag{A9}$$

here, f is a geometric factor, which is equal to $f = \frac{16\pi}{3}$ for homogeneous nucleation of spherical particles. The critical radius r_c for nucleation is then given by

$$r_c = \frac{2\gamma}{F} \tag{A10}$$

The steady state nucleation rate ($\dot{N}_{SS}$) is calculated according to the CNT:

$$\dot{N}_{SS} = \frac{1}{2}\rho^{\frac{3}{2}} Z\beta \exp\left(\frac{-\Delta G}{k_B T}\right) \tag{A11}$$

The term $\frac{1}{2}\rho^{\frac{3}{2}}$ represents the number of possible nucleation sites, with ρ being the dislocation density, Z the Zeldovich factor, β the atomic attachment rate, k_B the Boltzmann constant, and T the temperature in Kelvin. The Zeldovich factor corresponds to the curvature of ΔG at r_c and reflects the fluctuations of the critical radius according to Brownian motion.

$$Z = \sqrt{\frac{A\gamma}{9\pi k_B T}\frac{1}{n^{\frac{4}{3}}}} \tag{A12}$$

Since the gain and loss of ΔG for a nucleus is discretized in terms of the number of monomer units in the nucleus, Z also depends on the monomer number n, not on r. n can be calculated from r by the molar volume v_{mol}:

$$n = \frac{\frac{4}{3}\pi r_c^3}{\left(v_{\text{mol}} N_A\right)^{-1}} \tag{A13}$$

A is also a constant, linking the critical volume of the nucleus to the monomer number n:

$$A = \left(\frac{36\pi}{(v_{\mathrm{mol}} N_A)^{-2}}\right)^{\frac{1}{3}} \tag{A14}$$

The atomic attachment rate correlates the nucleus surface area with the diffusional flux through onto this area:

$$\beta = \frac{4\pi r_c^2}{a_0^4}\left[\frac{\left(c_i^p - c_i^0\right)^2}{c_i^0 D_i^0}\right]^{-1} \tag{A15}$$

D_i^0 represents the diffusion coefficient of element i in the matrix.

The steady state nucleation rate $\dot{N}_{SS}$ can further be modified by an incubation time to express the transient nucleation rate ($\dot{N}_{tr}$):

$$\dot{N}_{tr} = \dot{N}_{SS} exp\left(\frac{-\tau}{t}\right) \tag{A16}$$

here, t is the current time and τ is the incubation time, with:

$$\tau = \frac{1}{2\beta Z^2} \tag{A17}$$

The evolution of particles of phase p with time is given by the kinetics equation:

$$\dot{r} = \frac{F - \frac{2\gamma}{r_p}}{RTr_p}\left[\frac{\left(c_i^p - c_i^0\right)^2}{c_i^0 D_i^0}\right]^{-1} \tag{A18}$$

Appendix B

The calculation of the chemical potential from the Gibbs free energy is given by

$$\begin{aligned}\mu_i &= \left(\frac{\partial G}{\partial N_i}\right)_{T,P,N_{i\neq j}} = \frac{\partial c_i}{\partial N_i}\left(\frac{\partial G}{\partial c_i}\right)_{T,P,N_{i\neq j}} \\ &= G + \frac{\partial G}{\partial c_i} + \frac{\partial G}{\partial c_{Va}} - c_{Va}\frac{\partial G}{\partial c_{Va}} - \sum_{i=1}^{n} c_i \frac{\partial G}{\partial c_i}\end{aligned} \tag{B1}$$

The calculation of the derivative of the enthalpy from the Gibbs free energy:

$$\frac{\partial H}{\partial f_p} = \frac{\partial H}{\partial c_i}\frac{\partial c_i}{\partial f_p} = \left(\frac{\partial G}{\partial c_i} + T\frac{\partial S}{\partial c_i}\right)\frac{\partial c_i}{\partial f_p} \tag{B2}$$

with the entropy S equal to $S = \frac{\partial G}{\partial T}$. Due to the proportionality between f_p and $\sum \partial N_i$, the enthalpy can be expressed as

$$\frac{\partial H}{\partial N} = \sum \mu_i + T\frac{\partial S}{\partial N_i} = \sum \mu_i + T\frac{\partial}{\partial N_i}\left(\frac{\partial G}{\partial T}\right) \tag{B3}$$

with $\frac{\partial H}{\partial N} = \frac{\partial H_0}{\partial N} + \frac{\partial H_p}{\partial N}$, including $\lim_{f_p \to 0}$ and in analogy to the chemical potential this expression can be further simplified to:

$$\begin{aligned}\Delta H_{\mathrm{sol}} = G_0 + T\frac{\partial G_0}{\partial T} - G_p - T\frac{\partial G_p}{\partial T} - \sum_{i}^{n} \Delta c_i\left(\mu_i + T\frac{\partial}{\partial c_i}\frac{\partial G_0}{\partial T}\right) \\ + \sum_{j\neq i}^{n} \Delta c_j\left(\mu_j + T\frac{\partial}{\partial c_j}\frac{\partial G_0}{\partial T}\right)\end{aligned} \tag{B4}$$

here, Δc_i is the relative change of the matrix composition, of the elements that are not participating in precipitation.

Acknowledgements

The authors would like to express their sincere gratitude to Hongcai Wang, Alireza Parsa, and Gunther Eggeler from the Ruhr-University Bochum for their invaluable contributions to this work. Their expertise and assistance with the SEM, TEM, and STEM measurements were essential to the progress of this research. The authors greatly appreciate the insightful discussions they shared, which significantly deepened the understanding of the topic.

Open Access funding enabled and organized by Projekt DEAL.

Conflict of Interest

The authors declare no conflict of interest.

Data Availability Statement

Research data are not shared.

Keywords

kinetics, microalloyed steels, precipitates, titanium–niobium carbonitrides, thermodynamics

Received: April 7, 2025
Revised: September 5, 2025

[1] H. Meuser, F. Grimpe, S. Meimeth, C. J. Heckmann, C. Träger, *Trans. Tech. Publ.* **2005**, *500*, 565.
[2] H. Tamehiro, N. Yamada, H. Matsuda, *Trans. Iron Steel Instit. Jpn.* **1985**, *25*, 54.
[3] S. Vervynckt, K. Verbeken, *Int. Mater. Rev.* **2012**, *57*, 187.
[4] I. Tamura, H. Sekine, T. Tanaka, *Thermomechanical Processing of High-Strength Low-Alloy Steels*, Butterworth-Heinemann **2013**.
[5] T. Maki, T. Furuhara, N. Tsuji, S. Morito, G. Miyamoto, A. Shibata, *Tetsu-To-Hagane/J. Iron Steel Instit. Jpn.* **2014**, *100*, 1062.
[6] J. Zhao, Z. Jiang, *Prog. Mater. Sci.* **2018**, *94*, 174.
[7] R. Lumley, A. Morton, I. Polmear, in *Nanostructure Control of Materials*, Elsevier, Amsterdam/New York **2006**, pp. 219–250.
[8] A. J. Craven, K. He, L. A. J. Garvie, T. N. Baker, *Acta Mater.* **2000**, *48*, 3857.
[9] A. J. Craven, K. He, L. A. J. Garvie, T. N. Baker, *Acta Mater.* **2000**, *48*, 3869.
[10] I. E. J. J. J. Weiss, J. Jonas, *Metall. Trans. A* **1979**, *10*, 831.
[11] I. B. Timokhina, P. D. Hodgson, S. P. Ringer, R. K. Zheng, E. V. Pereloma, *Scr. Mater.* **2007**, *56*, 601.

[12] S. K. Mishra, S. Das, S. Ranganathan, *Mater. Sci. Eng. A* **2002**, *323*, 285.
[13] M. Béreš, T. E. Weirich, K. Hulka, J. Mayer, *Steel Res. Int.* **2004**, *75*, 753.
[14] J. Webel, H. Mohrbacher, E. Detemple, D. Britz, F. Mücklich, *J. Mater. Res. Technol.* **2022**, *18*, 2048.
[15] S. G. Hong, K. B. Kang, C. G. Park, *Scr. Mater.* **2002**, *46*, 163.
[16] J. Svoboda, F. D. Fischer, P. Fratzl, E. Kozeschnik, *Mater. Sci. Eng. A* **2004**, *385*, 166.
[17] E. Kozeschnik, *Mater. Sci. Eng. A* **2004**, *385*, 157.
[18] R. Radis, E. Kozeschnik, *Modell. Simul. Mater. Sci. Eng.* **2012**, *20*, 055010.
[19] Chinese Society for Metals (CSM), Chinese Academy of Engineering (CAE), S. Jin, Q. Chen, J. Bratberg, in *HSLA Steels 2015, Microalloying 2015 & Offshore Engineering Steels 2015: Conf. Proc.*, Springer, Berlin/New York **2016**, pp. 173–177.
[20] J. H. Jang, C. H. Lee, H. N. Han, H. K. D. H. Bhadeshia, D. W. Suh, *Mater. Sci. Technol.* **2013**, *29*, 1074.
[21] K. Xu, B. G. Thomas, R. O'malley, *Metallurg. Mater. Trans. A* **2011**, *42*, 524.
[22] Y. Zeng, W. Wang, *J. Mater. Sci.* **2008**, *43*, 874.
[23] P. Marynowski, A. Henryk, M. Glowacki, *J. Mater. Eng. Perform.* **2019**, *28*, 4018.
[24] P. Marynowski, M. Hojny, *Arch. Metall. Mater.* **2022**, 1117.
[25] J.-M. Liu, Z. G. Liu, *Solid State Comm.* **1998**, *105*, 517.
[26] N. Korepanova, L. Gu, M. Dima, H. Xu, *Chin. Phys. B* **2022**, *31*, 026103.
[27] E. J. Palmiere, C. M. Sellars, S. V. Subramanian, in *Proc. of the Int. Symp. of Niobium* **2001**, pp. 501–526.
[28] H. Wang, C. Somsen, G. Eggeler, E. Detemple, *Mater. Werkstofftech.* **2018**, *49*, 726.
[29] H. C. Wang, *J. Mater. Sci.* **2019**, *54*, 7307.
[30] A. Hegetschweiler, T. Staudt, T. Kraus, *J. Mater. Sci.* **2019**, *54*, 5813.
[31] A. Hegetschweiler, A.-R. Jochem, A. Zimmermann, J. Walter, T. Staudt, T. Kraus, *Part. Particle Syst. Charac.* **2021**, *38*, 2000236.
[32] H. P. Langtangen, *Finite Difference Methods for Diffusion Processes*, University of Oslo **2015**.
[33] M. Charleux, W. J. Poole, M. Militzer, A. Deschamps, *Metall. Mater. Trans. A* **2001**, *32*, 1635.
[34] J. Webel, A. Herges, D. Britz, E. Detemple, V. Flaxa, H. Mohrbacher, F. Mücklich, *Metals* **2020**, *10*, 243.
[35] B. Dutta, E. J. Palmiere, C. Michael Sellars, *Acta Mater.* **2001**, *49*, 785.
[36] K. Frisk, U. Borggren, *Metall. Mater. Trans. A* **2016**, *47*, 4806.
[37] H. Leitner, M. Bischof, H. Clemens, S. Erlach, B. Sonderegger, E. Kozeschnik, J. Svoboda, *Adv. Eng. Mater.* **2006**, *8*, 1066.
[38] N. H. Van Dijk, W. G. Bouwman, S. E. Offerman, M. Th Rekveldt, J. Sietsma, S. Van der Zwaag, A. Bodin, R. K. Heenan, *Metall. Mater. Trans. A* **2002**, *33*, 1883.
[39] A. Deschamps, C. R. Hutchinson, *Acta Mater.* **2021**, *220*, 117338.
[40] A. Costa E Silva, *Calphad* **2020**, *68*, 101720.
[41] M. Pudar, S. Zamberger, K. Spiradek-Hahn, R. Radis, E. Kozeschnik, *Steel Res. Int.* **2010**, *81*, 372.
[42] E. Kozeschnik, J. M. Vitek, *Calphad* **2000**, *24*, 495.
[43] B. Sonderegger, E. Kozeschnik, *Metall. Mater. Trans. A* **2010**, *41*, 3262.